Article

A large-scale magnetic field produced by a solar-like dynamo in binary neutron star mergers

Kenta Kiuchi [1,2] ✉, Alexis Reboul-Salze[1], Masaru Shibata [1,2] & Yuichiro Sekiguchi[2,3]

The merger of two neutron stars launches a relativistic jet, which must be driven by a strong large-scale magnetic field. However, the magnetohydrodynamical mechanism required to build up this magnetic field remains uncertain. By performing an ab initio super-high-resolution neutrino-radiation magnetohydrodynamics merger simulation in full general relativity, we show that the $\alpha\Omega$ dynamo mechanism, driven by the magnetorotational instability, builds up the large-scale magnetic field inside the long-lived remnant of the binary neutron star merger. As a result, the magnetic field induces a Poynting-flux-dominated relativistic outflow with an isotropic equivalent luminosity of $\sim 10^{52}$ erg s^{-1} and a magnetically driven post-merger mass ejection of $\sim 0.1\,M_\odot$. Therefore, the magnetar hypothesis, in which an ultra-strongly magnetized neutron star drives a relativistic jet in binary neutron star mergers, is possible. Magnetars can be the engines of short, hard gamma-ray bursts, and they should be associated with very bright kilonovae, which current telescopes could observe. Therefore, this scenario is testable in future observations.

The observation of GW 170817/GRB 170817A/AT 2017gfo made binary neutron star mergers a leading player of multi-messenger astrophysics[1–5]. It revealed that at least a part of the origin of short, hard gamma-ray bursts and the heavy elements synthesized by rapid neutron capture (the r process) is binary neutron star mergers[1–4,6–9].

All the fundamental interactions play an essential role in binary neutron star mergers. Thus, the method chosen to explore them theoretically is a numerical relativity simulation that implements all the effects of the fundamental interactions. Numerical relativity simulations can qualitatively explain AT 2017gfo, that is, the kilonova emissions associated with the radioactive decay of the r-process elements[10–18]. However, a quantitative understanding of this event is still being developed. Moreover, there is no theoretical consensus about how the binary neutron star merger drove the short, hard gamma-ray burst[19–21].

A relativistic jet was launched from this binary neutron star merger, which was observed as a short and hard gamma-ray burst[1–4]. Such relativistic jets are most likely driven by a magnetohydrodynamics process. This indicates that a binary neutron star merger remnant must build up a large-scale magnetic field with the dynamo to launch the jet[22,23]. However, the mechanism behind the large-scale dynamo in the merger remnant still needs to be clarified[24,25].

Also, the site for generating the large-scale magnetic field after the merger is a riddle. Is it inside a massive torus around a black hole that formed after a merger remnant collapsed into it? Or is it the long-lived remnant of a massive neutron star[26]? Recent numerical simulations for a black hole and torus system, as a remnant of a binary neutron star merger or a black hole–neutron star merger, suggest that a large-scale magnetic field is established after a long-term evolution of $O(1$–$10)$ s (refs. 20,27–29). Consequently, a relativistic jet is launched due to the

[1]Max Planck Institute for Gravitational Physics (Albert Einstein Institute), Potsdam, Germany. [2]Center for Gravitational Physics and Quantum Information, Yukawa Institute for Theoretical Physics, Kyoto University, Kyoto, Japan. [3]Department of Physics, Toho University, Chiba, Japan. ✉e-mail: kenta.kiuchi@aei.mpg.de
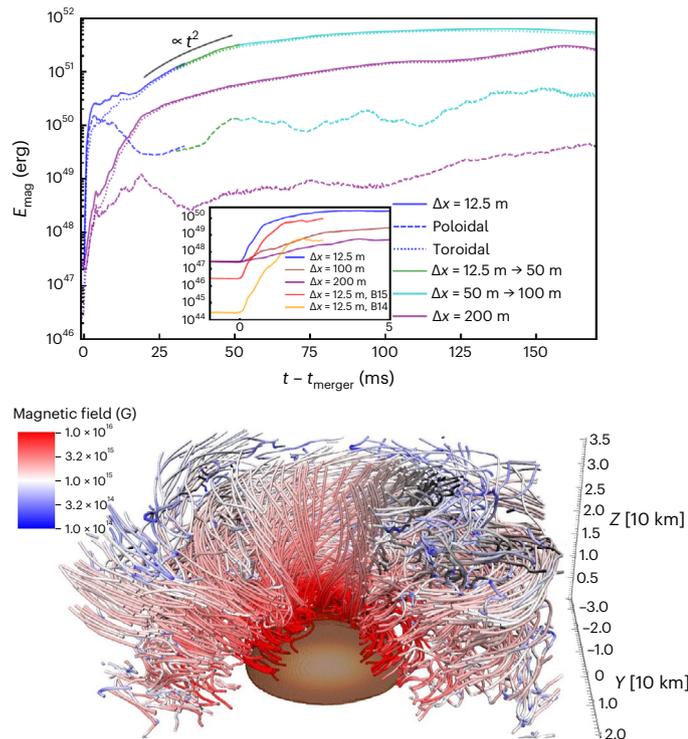
Fig. 1 | Overview of the magnetic field evolution in the remnant of the binary neutron star. Top, Electromagnetic energy as a function of the post-merger time for the total (solid), the poloidal (dashed) and the toroidal (dotted) components. The purple curves are for the simulation with $\Delta x_{finest} = 200$ m. The inset shows how the amplification of the magnetic field due to the Kelvin–Helmholtz instability depends on the initial magnetic field strength and grid resolution. B14 and B15 mean $B_{0,max} = 10^{14}$ G and 10^{15} G, respectively. Bottom, Magnetic field lines for a density of $\rho < 10^{13}$ g cm^{-3} at $t - t_{merger} \approx 130$ ms. The core of the hypermassive neutron star is shown for a density of $\rho > 10^{13}$ g cm^{-3}.
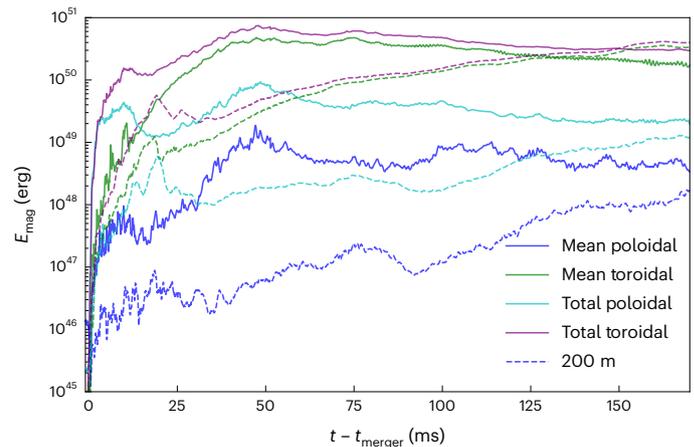
Fig. 2 | Generation of mean electromagnetic field. Mean and total electromagnetic energy in the region where the magnetorotational instability is active with $\rho \leq 10^{14.5}$ g cm^{-3} as a function of the post-merger time. The blue, green, cyan and purple curves denote the mean poloidal, mean toroidal, total poloidal and total toroidal components, respectively, in the high-resolution simulation. The dashed curves are for the simulation with $\Delta x_{finest} = 200$ m.

Blandford–Znajek mechanism[30]. However, the long-lived remnant of a massive neutron star is more computationally challenging than the black hole plus torus system because the requirement to resolve relevant magnetohydrodynamical instabilities numerically is severe[31]. The physical mechanism for generating the large-scale magnetic field and launching the jet could differ in the two scenarios mentioned above. It could be observationally testable if we managed to build a long-lived binary neutron start model that generates a large-scale B field and launches a jet.

We tackle this problem with a super-high-resolution neutrino-radiation magnetohydrodynamics simulation of a binary neutron star merger in full general relativity.

We employ the latest version of our numerical relativity neutrino-radiation magnetohydrodynamics code[32]. We employ a static mesh refinement with 2:1 refinements to cover a wide dynamic range. For the simulations in this article, the grid structure consists of 16 Cartesian domains. Each domain has $2N \times 2N \times N$ elements in the x, y and z directions, and we assume orbital plane symmetry. We set $N = 361$ and $\Delta x_{finest} = 12.5$ m. The grid resolution is the highest among the binary neutron star merger simulations[31]. The initial orbital separation is ~44 km (Methods).

We employ DD2 (ref. 33) as an equation of state for the neutron star matter and symmetric binary, which has a total mass of $2.7\,M_\odot$. With this set-up, a hypermassive neutron star that transiently formed after the merger will survive for $>O(1)$ s (ref. 34).

The purely poloidal magnetic field loop is embedded inside the neutron stars and has a maximum field strength of $B_{0,max} = 10^{15.5}$ G (ref. 35). It is much stronger than the 10^7–10^{11} G observed for binary

pulsars (ref. 36). The available computational resources limit us to a strong field strength and idealized topology. Nonetheless, it is natural to anticipate that in reality the amplification of the magnetic field leads to a high field strength ($>10^{16}$ G) in a short timescale after the merger (see below).

Figure 1 plots the evolution of the electromagnetic energy as a function of the post-merger time. As reported in refs. 31,35, the electromagnetic energy was exponentially amplified shortly after the merger due to the Kelvin–Helmholtz instability, which emerges at the contact interface when the binary merges. A part of the turbulent kinetic energy due to the instability is converted to electromagnetic energy[35]. In the inset, we generate the same plot for $-1 \leq t - t_{merger} \leq 5$ ms but different initial magnetic field strengths of $B_{0,max} = 10^{15}$ G (red) and $B_{0,max} = 10^{14}$ G (orange) while keeping the grid resolution. Also, we plot the results for the other grid resolutions of $\Delta x_{finest} = 100$ or 200 m (brown and purple curves, respectively), while keeping $B_{0,max} = 10^{15.5}$ G. The figure clearly shows that the growth rate of the electromagnetic energy for $0 \lesssim t - t_{merger} \lesssim 1$ ms does not depend on the initial field strength but on the grid resolution, as expected from the properties of the Kelvin–Helmholtz instability[37,38] (Extended Data Fig. 1). The post-merger amplification of the magnetic field due to this instability terminates when the shear layer is dissipated by the shock waves at $t - t_{merger} \approx 2$ ms.

At $t - t_{merger} \approx 5$ ms, the electromagnetic energy temporarily settles to ~3×10^{50} erg. However, the toroidal magnetic field (dotted curve) is subsequently amplified. In particular, its contribution to the total electromagnetic energy becomes prominent for $t - t_{merger} \gtrsim 20$ ms and the growth rate is proportional to t^2, which indicates that the magnetic winding is efficient with a coherent poloidal magnetic field. The differential rotational energy of ~1–2×10^{53} erg of the remnant of the massive neutron star is the energy budget for the magnetic winding. Once the magnetic braking starts to work, the electromagnetic energy saturates around ~5×10^{51} erg. We also plot the result of the simulation with $\Delta x_{finest} = 200$ m in Fig. 1. With this resolution, it is hard to resolve the Kelvin–Helmholtz and magnetorotational instability, particularly in the high-density region (Extended Data Figs. 1–3, and the section on convergence in Methods). Consequently, the amplification of the electromagnetic energy is less efficient in the low-resolution case. In particular, there is a striking difference in the poloidal magnetic field between the simulations with $\Delta x_{finest} = 12.5$ and 200 m. Because the magnetic field that is amplified due to the Kelvin–Helmholtz instability
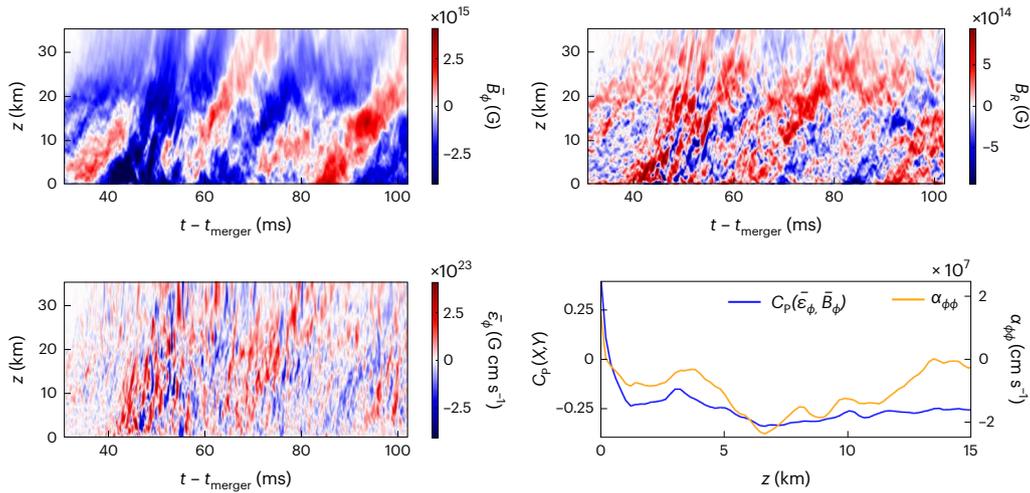
Fig. 3 | $\alpha\Omega$ dynamo inside the remnant of the binary neutron star merger. Butterfly diagrams at $R = 30$ km. Top left, Mean toroidal magnetic field $\bar{B}_\phi$. Top right, Mean radial magnetic field $\bar{B}_R$. Bottom left, Toroidal electromotive force $\bar{\mathcal{E}}_\phi$. Bottom right, Parameters $\alpha_{\phi\phi}$ (orange) and correlation between $\bar{\mathcal{E}}_\phi$ and $\bar{B}_\phi$ (blue).

Table 1 | The $\alpha\Omega$ dynamo period prediction and simulation data at several radii

R (km)	$\alpha_{\phi\phi}$ (cms^{-1})	Ω (rads^{-1})	Shear rate	k_z (cm^{-1})	P_{theory} (s)	P_{sim} (s)
20	-8.1×10^6	4,025	$q=1.00$	6.3×10^{-6}	0.020	0.018
30	-1.0×10^7	2,515	$q=1.34$	4.2×10^{-6}	0.021	0.018–0.024
40	-1.0×10^7	1,688	$q=1.44$	3.3×10^{-6}	0.037	0.018–0.030
50	-4.4×10^6	1,200	$q=1.50$	2.6×10^{-6}	0.062	0.030–0.040

P_{theory}, the $\alpha\Omega$ dynamo period; P_{sim}, the Butterfly diagram period in the simulation.

is randomly oriented[31], there must be a mechanism to generate the coherent poloidal magnetic field.

To make it clear which part of the merger remnant is responsible for the generation of the coherent magnetic field, we evaluate the electromagnetic energy in the region where the magnetorotational instability is active, as defined by $\rho \leq 10^{14.5}$ g cm^{-3} and as shown in Fig. 2 (Extended Data Fig. 2). We also decompose the contributions from the mean poloidal and toroidal magnetic fields by taking an axisymmetric average. The electromagnetic energy in this region is subdominant compared to that contained deep inside the core region where $\rho \geq 10^{14.5}$ g cm^{-3} (see also Fig. 1). However, in the simulation with $\Delta x_{finest} = 12.5$ m, the mean poloidal field exponentially grows in the range $20 \lesssim t - t_{merger} \lesssim 50$ ms. At $t - t_{merger} \approx 20$ ms, its contribution to the total poloidal field energy (solid cyan curve) is ~1% and becomes ~10% after the exponential growth. Such a clear exponential growth is invisible in the simulation with $\Delta x_{finest} = 200$ m for $t - t_{merger} \lesssim 100$ ms. Also, the mean poloidal field energy differs by one or two orders of magnitude in the simulations with $\Delta x_{finest} = 12.5$ or 200 m. For the toroidal component, the mean and total field energy are of the same order of magnitude for $t - t_{merger} \gtrsim 30$ ms. We also confirm that the magnetorotational instability is responsible for generating the mean poloidal magnetic flux (Extended Data Figs. 4 and 5). These results indicate that the generation of a coherent magnetic field is triggered by the magnetorotational instability.

The $\alpha\Omega$ dynamo, which is driven by the magnetorotational instability[39] in the current context, is a potential mechanism for generating the large-scale magnetic field[22,23]. In the mean field dynamo theory, we assume that each physical quantity Q is composed of the mean field $\bar{Q}$

and the fluctuation q, that is, $Q = \bar{Q} + q$. Thus, we cast the induction equation as

$$\partial_t \bar{\mathbf{B}} = \nabla \times \left(\bar{\mathbf{U}} \times \bar{\mathbf{B}} + \bar{\mathcal{E}} \right), \tag{1}$$

where $\bar{\mathcal{E}} = \overline{\mathbf{u} \times \mathbf{b}}$ is the electromotive force due to the fluctuations, $\mathbf{B} = \bar{\mathbf{B}} + \mathbf{b}$ is the magnetic field and $\mathbf{U} = \bar{\mathbf{U}} + \mathbf{u}$ is the velocity field. Note that the magnetorotational instability-driven turbulence produces the fluctuations $\mathbf{u}$ and $\mathbf{b}$. In the $\alpha\Omega$ dynamo, we express the electromotive force as a function of the mean magnetic field:

$$\bar{\mathcal{E}}_i = \alpha_{ij}\bar{B}_j + \beta_{ij}\left(\overline{\nabla \times \bar{B}} \right)_j, \tag{2}$$

where α_{ij} and β_{ij} are tensors that do not depend on $\bar{B}_j$. We calculate the mean field by taking the average in the azimuthal direction.

In the presence of a cylindrical differential rotation, the simplest mean field dynamo is an $\alpha\Omega$ dynamo, in which the toroidal magnetic field is generated by the shear of the poloidal magnetic field by the differential rotation $\bar{U}_\phi$, which is also called the Ω effect. The decrease in the rotation with radius and equation (1) imply that $\bar{B}_\phi$ should be anti-correlated with $\bar{B}_R$. To complete the dynamo cycle, the poloidal magnetic field has to be generated by the toroidal electromotive force $\bar{\mathcal{E}}_\phi$, whose main contribution is from a diagonal component $\alpha_{\phi\phi}$, which is the so-called α effect. $\bar{\mathcal{E}}_\phi$ is, therefore, correlated or anti-correlated to $\bar{B}_\phi$ depending on the sign of $\alpha_{\phi\phi}$ (equation (2)). This complete cycle forms a dynamo wave that oscillates with a period of $P_{theory} = 2\pi \left| \frac{1}{2} \alpha_{\phi\phi} \frac{d\Omega}{d\ln R} k_z \right|^{-1/2}$ (refs. 22,23) and propagates in the direction $\alpha_{\phi\phi} \nabla\Omega \times e_\phi$ according to the Parker–Yoshimura rule[40,41]. Here k_z is the wavenumber of the dynamo wave in the vertical direction. In this theoretical description, we have supposed that contributions from the other α_{ij} components and the turbulent resistivity tensor β_{ij} are subdominant. We will show that it is the case in the following.

First, we confirm that the simulation set-up employed can capture the fastest-growing mode of the magnetorotational instability in the outer region of the hypermassive neutron star (Extended Data Fig. 2). Therefore, the turbulent state is developed. Figure 3 plots the butterfly diagrams for $\bar{B}_\phi$, $\bar{B}_R$ and $\bar{\mathcal{E}}_\phi$ at $R = 30$ km. The top left and top right panels show the anti-correlation between $\bar{B}_\phi$ and $\bar{B}_R$, which indicates the Ω effect. To quantify the correlation between $\bar{B}_\phi$ and $\bar{\mathcal{E}}_\phi$, we compute the Pearson correlation $C_P(X, Y)$ between the two quantities X and Y in the bottom right panel of Fig. 3. This figure shows that $\bar{B}_\phi$ and $\bar{\mathcal{E}}_\phi$ are anti-correlated for $z \lesssim 15$ km, where the pressure scale height at
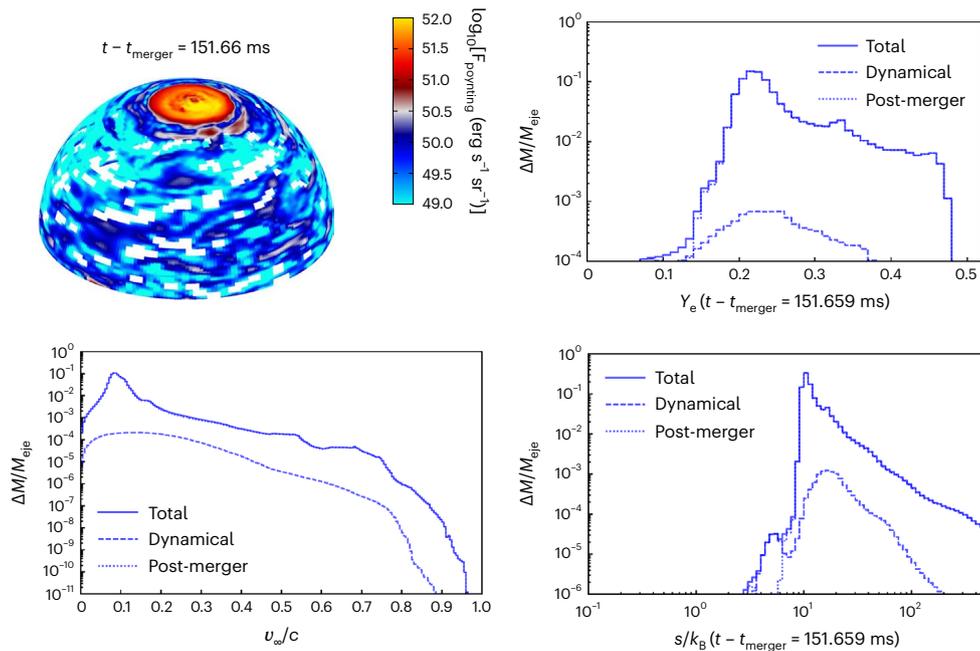
Fig. 4 | Electromagnetic signals from the remnants of the binary neutron star merger. Top left, Angular distribution of the Poynting flux on a sphere with $r \approx 500$ km at $t - t_{merger} \approx 150$ ms. Top right, Electron fraction distribution for the magnetically driven post-merger ejecta (dashed) and the dynamical ejecta (dotted). Bottom, Same as the top right panel but for the terminal velocity (left) and entropy per baryon (right).

$R = 30$ km is ~14.6 km. The correlation between the electromotive force and mean current $\bar{J}_i = \left(\overline{\nabla \times B}\right)_i$ is small, and thus, the β_{ij} tensor can be neglected (Extended Data Fig. 6). Therefore, the generation of the mean poloidal magnetic field is determined primarily by the α_{ij} tensor. Although $\alpha_{\phi R}$ has a non-negligible contribution, the contribution of $\alpha_{\phi\phi}B_\phi$ dominates in the turbulent region for $z \lesssim 10$ km (Extended Data Fig. 6). This shows that $\alpha_{\phi\phi}$ is the main component, and it is plotted in the bottom right panel of Fig. 3. We also confirmed that the $\alpha^2\Omega$ dynamo is irrelevant compared to the $\alpha\Omega$ dynamo (Extended Data Fig. 7).

With these quantities, we can predict the period of the $\alpha\Omega$ dynamo, as listed in Table 1. We measured the shear rate $q = -d\ln \Omega / d\ln R$ at the selected radius and choose the wavenumber k_z corresponding to the pressure scale height, which is the most extended vertical length in the turbulent region. The sixth and seventh columns report the predicted period of the $\alpha\Omega$ dynamo and the period measured in the butterfly diagram. The agreement at $R = 30$ km is remarkable. We show the comparison at different radii from $R = 20$ to 50 km in the table, and the agreement is also reasonable. In addition, since $\alpha_{\phi\phi}$ is negative and q is positive, the dynamo wave propagates along the direction of the Parker–Yoshimura rule, that is, the z direction (http://www2.yukawa.kyoto-u.ac.jp/~kenta.kiuchi/anime/SAKURA/Br_core_cut_9km.m4v). With these findings, we conclude that the dynamo in our simulation can be interpreted as an $\alpha\Omega$ dynamo, and it builds up the large-scale magnetic field in the remnant of the hyper-massive neutron star (Fig. 1).

After the development of the coherent poloidal magnetic field due to the $\alpha\Omega$ dynamo and the resultant efficient magnetic winding, a magnetic-tower outflow is launched towards the polar direction (http://www2.yukawa.kyoto-u.ac.jp/~kenta.kiuchi/anime/SAKURA/DD2_135_135_Dynamo.mp4; Methods). The mean poloidal magnetic flux is generated in the region where the magnetorotational instability is active. The mean magnetic field deep inside the core ($\rho \geq 10^{14.5}\,g\,cm^{-3}$), which could be a relic of the initial field, stays buried below $r \lesssim 10$ km in the polar region throughout the simulation (http://www2.yukawa.kyoto-u.ac.jp/~kenta.kiuchi/anime/SAKURA/movie_Mean_Poloidal_Flux.mp4; Methods). This indicates that the large-scale field generated

by the $\alpha\Omega$ dynamo is responsible for launching the jet. We confirm that the low-resolution simulation cannot capture the launching of the strong Poynting-flux-dominated outflow or the enormous post-merger ejecta[21] (see also Extended Data Fig. 8).

The luminosity of the Poynting flux, which is defined by $L_{Poy} = -\oint_{r\approx 500km} \sqrt{-g}\, (T^r{}_t)_{(EM)}\, d\Omega$, where $T^{\mu\nu}_{(EM)}$ is the stress energy tensor for the electromagnetic field, is ~10^{51} erg s^{-1} at the end of the simulation when $t - t_{merger} \approx 150$ ms. The high Poynting flux is confined in the region with $\theta \lesssim 12°$ where θ is a polar angle, as plotted in the top left panel of Fig. 4 (see also Extended Data Fig. 8). The luminosity and jet opening angle are broadly compatible with some of the observed short, hard gamma-ray bursts[42]. We estimate the terminal Lorentz factor Γ_∞ by the magnetization parameter $\sigma_{LC} = b^2/4\pi\rho c^2$ at the light cylinder radius $r_{LC} = c/\Omega \approx 40$ km $((\Omega/7,000\,rad\,s^{-1})^{-1})$ contained in a region $\theta < 12°$ (refs. 43,44). We found the baryon loading is still severe, for example, $\dot{M}_{outflow} \approx 10^{-2}\,M_\odot\,s^{-1}$ in the polar region. Nonetheless, Γ_∞ increases with time but fluctuates. It reaches ~10–20 at the end of the simulation. Therefore, if the magnetic reconnection efficiently dissipated the Poynting flux, a Lorentz factor of ~10 could be possible[44]. Also, the evacuation due to the strong Poynting flux in the polar region continues at the end of the simulation. Therefore, a higher Γ_∞ could be possible after the long-term evolution.

The dynamical ejecta driven by the tidal force and the shock wave during the merger phase represent ~0.002 $M_\odot$ (ref. 34). After the development of the coherent magnetic field, we observe a new component in the ejecta that is driven by the Lorentz force, namely, the magnetically driven wind[45]. The mass of this component is ~0.1 $M_\odot$ at the end of the simulation $t - t_{merger} \approx 150$ ms. The electron fraction of the post-merger ejecta shows a peak around ~0.2 with an extension to ~0.5. The terminal velocity of the post-merger ejecta peaks around ~0.08c, where c is the speed of light. Therefore, it could contribute to a bright kilonova emission through the synthesis of r-process heavy elements[26,46].

We speculate that the high-luminosity state and the post-merger mass ejection would continue for $O(1)$ s, which corresponds to the neutrino cooling timescale[34,47]. As reported in refs. 27,34, the torus expands due to the angular momentum transport facilitated by the magnetorotational instability-driven turbulent viscosity after the

neutrino cooling becomes inefficient. As a result, the funnel region above the remnant neutron star expands and the jet could no longer be collimated. A long-term simulation for $O(1)$ s of a remnant of a massive neutron star is future work to be pursued.

Also, a simulation with initially weakly magnetized binary neutron stars is necessary to confirm the picture reported in this article because the saturated magneto-turbulent state and the generation timescale of the coherent poloidal magnetic field due to the magnetorotational instability could depend on the initial magnetic field strength and flux[48]. The recent large-eddy simulations of a magnetized binary neutron star merger may give a hint about this issue[49,50]. Even if the initial magnetic field has a much weaker strength or different topology from the one we assumed, the saturation strength and field profile due to the Kelvin–Helmholtz instability in the merger remnant are like those that we found in this article. Also, how the mean poloidal magnetic field is set in reality after the merger is an open problem. If the mean poloidal magnetic field just after the merger is a relic of the pre-merger poloidal field, that is, 10^{10}–10^{11} G at maximum, it may take $\ln(10^4) \times 0.02$ s ≈ 0.2 s to reach the saturation strength of 10^{14}–10^{15} G, as we assume the mean poloidal field is exponentially amplified with the period of the $\alpha\Omega$ dynamo[22] (Fig. 2 and Table 1). Consequently, the jet may be launched at $O(0.1)$ s after the merger in reality. However, the interior structure of the magnetic field in the pre-merger neutron stars is not well understood, and the magnetic reconnection of the fluctuating poloidal field generated by the Kelvin–Helmholtz instability may enhance the mean poloidal field after the merger. This situation should be explored as a future task.

To summarize, we generated a large-scale magnetic field in a long-lived remnant of a binary neutron star merger using a super-high-resolution neutrino-radiation magnetohydrodynamics simulation in general relativity. The magnetorotational instability-driven $\alpha\Omega$ dynamo generates the large-scale magnetic field. As a result, the launch of the Poynting-flux-dominated relativistic outflow in the polar direction and an enormous amount of magnetically driven wind are induced. Our simulation suggests that the magnetar engine generates short, hard gamma-ray bursts and bright kilonovae emission, which could be observed in the near-future multi-messenger observations.

Methods
Numerical method
Our code implements the Baumgarte–Shapiro–Shibata–Nakamura-puncture formulation to solve Einstein's equation[51–54]. The code also uses the Z4c prescription to suppress the constraint violation[55]. The fourth-order accurate finite difference is used as a discretization scheme in space and time. The sixth-order Kreiss–Oliger dissipation is also employed. The HLLD Riemann solver[56] and the constrained transport scheme[57] are used to solve the equations of motion of the relativistic magnetohydrodynamic fluid. The neutrino-radiation transfer is solved by the grey M1+GR-leakage scheme[58] to take into account neutrino cooling and heating.

Initial data
We adopted quasi-equilibrium initial data of irrotational binary neutron stars in the neutrino-free beta equilibrium derived in a previous paper[34] using the public spectral library LORENE (ref. [59]). The initial orbital angular velocity is $Gm_0\Omega_0/c^3 \approx 0.028$ with $m_0 = 2.7\,M_\odot$. The residual orbital eccentricity is ~10^{-3}. For our high-resolution study, the data are remapped onto the computational domain described in the 'Grid set-up' section.

Grid set-up. We employ the static mesh refinement with 2:1 refinement, that is, a coarser domain with a grid resolution twice that of a finer domain. All the domains are composed of concentric Cartesian domains with a fixed grid size N. The size of the grid is $2N \times 2N \times N$ in the x, y and z directions, and we assume orbital plane symmetry. We employ 16 domains with $N = 361$ and the finest grid resolution of $\Delta x_\text{finest} = 12.5$ m. The first three finest domains, whose sizes are $[-4.5: 4.5\text{ km}]^2 \times [0: 4.5\text{ km}]$, $[-9: 9\text{ km}]^2 \times [0: 9\text{ km}]$ and $[-18: 18\text{ km}]^2 \times [0: 18\text{ km}]$, respectively, are employed to resolve the Kelvin–Helmholtz instability, which emerges on a contact interface (shear layer) when the two neutron stars merge. The initial binary separation is ~44 km, and the coordinate radius of the neutron star is 10.9 km. Thus, the fourth finest domain with $[-36: 36\text{ km}]^2 \times [0: 36\text{ km}]$ covers the entire binary neutron star.

We started each simulation with $\Delta x_\text{finest} = 12.5$ m and 16 static mesh refinement domains. At ~30 ms after the merger, we removed the two finest domains with $\Delta x_\text{finest} = 12.5$ m and $\Delta x = 25$ m and continued the simulation with $\Delta x_\text{finest} = 50$ m until ~50 ms after the merger. Then, we removed the domain with $\Delta x_\text{finest} = 50$ m and continued the simulation with $\Delta x_\text{finest} = 100$ m. The timing for removing the finer domains was determined by monitoring the magnetorotational instability quality factor so as not to go below the critical value of 10 after the removal (see below). This strategy allowed us to capture the efficient amplification of the magnetic field through the Kelvin–Helmholtz instability and resolve the magnetorotational instability inside the remnant while saving computational costs.

To check the validity of removing finer domains, we continued the simulation with $\Delta x_\text{finest} = 12.5$ m up to $t - t_\text{merger} \approx 33$ ms (see the blue dashed curve in Fig. 1). We observed an ~10% decrease in the poloidal electromagnetic energy in the simulation with $\Delta x_\text{finest} = 50$ m compared to that with $\Delta x_\text{finest} = 12.5$ m around this time. Nonetheless, the poloidal electromagnetic energy increased around $t - t_\text{merger} \approx 40$ ms in the simulation with $\Delta x_\text{finest} = 50$ m (the green dashed curve in Fig. 1) due to the α effect we discuss in the main text. Also, there was no substantial decrease in the toroidal electromagnetic energy after removing the finer domains at $t - t_\text{merger} \approx 30$ ms. Similarly, there was no visible deterioration after the second removal of the finer domain at $t - t_\text{merger} \approx 50$ ms.

For the convergence test, we also performed the simulations with $\Delta x_\text{finest} = 100$ (200) m and $N = 361$ (185). The number of domains was 13.

Equation of state. We extended the original DD2 equation of state to the low-density and temperature region with the Helmholtz equation of state[60]. Because any high-resolution shock-capturing scheme does not allow a vacuum state, we employed the atmospheric prescription outside the neutron stars. Specifically, we set a constant atmospheric density of 10^3 g cm^{-3} inside $r \leq L_\text{atm}$ and assumed a power-law profile $\rho_\text{atm} = \max[10^3 (L_\text{atm}/r)^3\text{ g cm}^{-3}, \rho_\text{fl}]$ for $r > L_\text{atm}$ where $L_\text{atm} = 36$ km. The Helmholtz equation of state employed determines the floor value of the rest-mass density, which is $\rho_\text{fl} = 0.167$ g cm^{-3}. We also assumed a constant atmospheric temperature of 10^{-3} MeV.

Kelvin–Helmholtz instability
The top panel of Extended Data Fig. 1 is the same as the inset in Fig. 1 but with additional data. The solid blue, solid brown and solid purple curves are the results with $\Delta x_\text{finest} = 12.5$, 100 and 200 m, respectively, with $B_{0,\text{max}} = 10^{15.5}$ G. The solid red and solid orange curves show the results with $\Delta x_\text{finest} = 12.5$ m with $B_{0,\text{max}} = 10^{15}$ and 10^{14} G, respectively. The cyan curve shows the result with $\Delta x_\text{finest} = 18.75$ m and $B_{0,\text{max}} = 10^{14}$ G. The dotted blue and dotted red curves plot the result with $\Delta x_\text{finest} = 12.5$ m and $B_{0,\text{max}} = 10^{14}$ G magnified by the square of the ratio of the initial magnetic field strength, that is, $(10^{15.5}/10^{14})^2 = 10^3$ and $(10^{15}/10^{14})^2 = 10^2$, respectively.

This figure suggests the following two points. First, the solid and dotted blue curves and the solid and dotted red curves overlap until the back reaction starts to activate, which happens when the electromagnetic energy reaches ~3×10^{49} erg. This implies that the magnetic field is passive for $t - t_\text{merger} \lesssim 1$ ms, which is the linear phase. The saturation of the electromagnetic energy due to the Kelvin–Helmholtz instability is likely to be ~1–3×10^{50} erg corresponding to $O(0.1)\%$ of the internal energy[31,50,61,62].

The second point is that the growth rate of the electromagnetic energy in the linear phase depends on the grid resolution not on the initial magnetic field strength. To quantify the dependence of the growth rate on the grid resolution and initial magnetic field strength, we estimated the growth rate by fitting the electromagnetic energy as $E_{mag}(t) = A \exp(\sigma_{KH}(t - t_{merger}))$ for $0 \lesssim t - t_{merger} \lesssim 1$ ms, which corresponds to the linear phase. The bottom panel of Extended Data Fig. 1 plots the estimated growth rate as a function of the initial magnetic field strength. The symbols denote the grid resolution. With $\Delta x_{finest} = 12.5$ m, the growth rate was ~7 ms^{-1}, irrespective of the initial magnetic field strength. The growth rate increased with the grid resolution. With $\Delta x_{finest} = 100$ or 200 m, the efficient amplification cannot be captured. All the properties are consistent with those of the Kelvin–Helmholtz instability, that is, the smaller the scale of the vortices is, the larger the growth rate is[63]. The reality is located in the leftward and upward direction in this diagram, that is, the weak magnetic field observed in binary pulsars (the leftward direction in the diagram) and infinitesimal grid resolution (the upward direction in the diagram). Therefore, we anticipate that the electromagnetic energy will saturate in a very short timescale, ≪1 ms after the binary neutron star merger, irrespective of the magnetic field strength at the onset of the merger unless a black hole is promptly formed[31,35,64].

We estimated how small Δx_{finest} should be to simulate the amplification due to the Kelvin–Helmholtz instability starting from the 'realistic' initial magnetic field strength of 10^{11} G (ref. 36). The saturation strength found in the simulation with $\Delta x_{finest} = 12.5$ m is likely to be $|\bar{B}| \approx 10^{16.5}$ G. We fitted the growth rate as a function of the grid resolution from Extended Data Fig. 1. It was $\sigma_{KH}(ms^{-1}) = 90/\Delta x_{finest}(m)$, where we assumed the inverse proportionality would originate due to the Kelvin–Helmholtz instability[37,38]. Assuming that the initial magnetic field strength was 10^{11} G and that the lifetime of the shear layer was 2 ms, we estimated the required growth rate as

$$\sigma_{KH} = \frac{1}{2\,ms} \ln\left(\frac{10^{16.5}\,G}{10^{11}\,G}\right)^2 = 12.7\,ms^{-1}. \tag{3}$$

Therefore, the required grid resolution is

$$\Delta x_{finest} = \frac{90}{\sigma_{KH}} \approx 7.1\,m. \tag{4}$$

Magnetorotational instability, neutrino viscosity and neutrino drag

To quantify how well the magnetorotational instability is resolved in our simulation, we estimated the rest-mass-density-conditioned magnetorotational instability quality factor, as defined by

$$\langle Q_{MRI}\rangle_\rho \equiv \frac{\langle \lambda_{MRI}\rangle_\rho}{\Delta x} = \frac{1}{\Delta x}\frac{\int_\rho \lambda_{MRI}\,d^3x}{\int_\rho d^3x}, \tag{5}$$

where $\lambda_{MRI} = 2\pi B^z/(\sqrt{4\pi\rho}\,\Omega)$ is the fastest-growing mode of an ideal magnetorotational instability[39]. As the condition in terms of the rest-mass density, we define a remnant core and a remnant torus as fluid elements with $\rho \geq 10^{13}$ and $<10^{13}$ g cm^{-3}, respectively. Furthermore, we exclude the core region above $10^{14.5}$ g cm^{-3} in the estimate of the quality factor because in such a region, the radial gradient of the angular velocity is positive, and it is not subject to magnetorotational instability[39], as plotted in the top panel of Extended Data Fig. 2. Also, we introduce a cutoff density of 10^7 g cm^{-3} for the torus to suppress the overestimation of the quality factor in the low-density polar region. The middle and bottom panels of the figure show that the fastest-growing mode of the magnetorotational instability is well resolved, both in the core and torus, throughout the simulation. Consequently, magneto-turbulence develops and is sustained. However, the magnetorotational instability, particularly in the core throughout

the entire simulation and in the torus for $t - t_{merger} \lesssim 80$–90 ms, cannot be resolved when $\Delta x_{finest} = 200$ m. Thus, the turbulence is not fully produced in such a low-resolution run.

One caveat is that the neutrino viscosity and drag could affect the magnetorotational instability as diffusive and damping processes[65]. The former (latter) becomes relevant when the neutrino mean free path is shorter (longer) than the wavelength of the magnetorotational instability. Given a profile of the merger remnant, such as the density ρ, angular velocity Ω, temperature T and hypothetical magnetic field strength B^z_{hyp}, we solve the two branches of the dispersion relations to quantify the neutrino viscosity and drag effects[65]: For the neutrino viscosity:

$$\left[\left(\tilde{\sigma} + \tilde{k}^2\tilde{\nu}_\nu\right)\tilde{\sigma} + \tilde{k}^2\right]^2 + \tilde{\kappa}^2\left[\tilde{\sigma}^2 + \tilde{k}^2\right] - 4\tilde{k}^2 = 0, \tag{6}$$

and for the neutrino drag:

$$\left[\left(\tilde{\sigma} + \tilde{\Gamma}_\nu\right)\tilde{\sigma} + \tilde{k}^2\right]^2 + \tilde{\kappa}^2\left[\tilde{\sigma}^2 + \tilde{k}^2\right] - 4\tilde{k}^2 = 0, \tag{7}$$

where $\tilde{\sigma} = \sigma/\Omega, \tilde{k} = kv_A/\Omega, \tilde{\kappa}^2 = \kappa^2/\Omega^2, \tilde{\nu}_\nu = \nu_\nu\Omega/v_A^2$ and $\tilde{\Gamma}_\nu = \Gamma_\nu/\Omega$. σ and k are the growth rate and wavenumber of the unstable mode of the magnetorotational instability. $v_A = B^z_{hyp}/\sqrt{4\pi\rho}$ is the Alfvén wave speed. κ^2 is the epicyclic frequency. ν_ν and Γ_ν are the neutrino viscosity and drag damping rate, respectively. Reference [65] provides fitting formulae for them as functions of the rest-mass density and temperature:

$$\nu_\nu = 1.2 \times 10^{10}\left(\frac{\rho}{10^{13}\,g\,cm^{-3}}\right)^{-2}\left(\frac{T}{10\,MeV}\right)^2 cm^2\,s^{-1}, \tag{8}$$

$$\Gamma_\nu = 6 \times 10^3\left(\frac{T}{10\,MeV}\right)^6 s^{-1}. \tag{9}$$

Also, the neutrino mean free path l_ν is fitted by

$$l_\nu = 2 \times 10^3\left(\frac{\rho}{10^{13}\,g\,cm^{-3}}\right)^{-1}\left(\frac{T}{10\,MeV}\right)^{-2} cm. \tag{10}$$

Extended Data Fig. 3 plots the growth rate of the magnetorotational instability for a given profile of a remnant of a massive neutron star and a hypothetical value of B^z_{hyp}. We use the profiles on the orbital plane at $t - t_{merger} \approx 10$ ms. The purple curve denotes the boundary where the condition $\tilde{\nu}_\nu$ or $\tilde{\Gamma}_\nu \approx 1$ is met[65]. Inside the boundary, the neutrino viscosity or the neutrino drag substantially suppresses the growth rate. Outside it, the growth rate is essentially the same as for the ideal magnetorotational instability. Above it, we plot the azimuthally averaged magnetic field strength $\bar{B}^z_{sim}$ obtained in the simulation. Because of the efficient amplification due to the Kelvin–Helmholtz instability just after the merger, the neutrino viscosity and drag effects are irrelevant in the entire region of the merger remnant.

Generation of mean poloidal magnetic flux due to the magnetorotational instability

To validate our interpretation that the $\alpha\Omega$ dynamo is responsible for generating the large-scale magnetic field, we evaluate the mean poloidal magnetic flux on a certain sphere of radius r:

$$\Phi_{\bar{B}_r}(r) = 2\int_0^{\pi/2}\bar{B}_r r^2 \sin\theta\,d\theta, \tag{11}$$

where $\bar{B}_r$ denotes the radial mean field in the spherical-polar coordinate.

Extended Data Fig. 4 plots the evolution of the mean poloidal magnetic flux. We selected 8 and 20 km as representative radii for the

magnetorotational instability inactive and active regions (see the top panel of Extended Data Fig. 2). On the one hand, in the simulation with $\Delta x_{\text{finest}} = 12.5$ m, the mean poloidal magnetic flux on the sphere with $r = 8$ km exhibits intensive time variability for $t - t_{\text{merger}} \lesssim 20$ ms, which reflects the oscillations of the remnant core, that is, compression and decompression. The poloidal flux gradually decreases, presumably due to the magnetic reconnection, which is imprinted as the decrease of the total poloidal field energy for $10 \lesssim t - t_{\text{merger}} \lesssim 20$ ms in Fig. 1. Nonetheless, it relaxes to a roughly constant value and stays there until $t - t_{\text{merger}} \lesssim 120$ ms. This reflects that magnetorotational instability is inactive in this region, that is, the mean poloidal magnetic flux is not generated. On the other hand, it is evident that the mean poloidal flux on the sphere with $r = 20$ km is generated around $t - t_{\text{merger}} \approx 25$ ms in the high-resolution simulation. Such efficient generation of the mean poloidal flux is not observed in the simulation with $\Delta x_{\text{finest}} = 200$ m for $t - t_{\text{merger}} \lesssim 80$ ms, as plotted with the green dashed curve in the figure (but see below for details about the slight generation of the mean poloidal flux for $40 \lesssim t - t_{\text{merger}} \lesssim 60$ ms). For $t - t_{\text{merger}} \gtrsim 100$ ms, the mean poloidal magnetic flux is generated even in the low-resolution simulation because the magnetorotational instability starts to be partially, not fully, resolved in the low-density region (see the middle and bottom panels of Extended Data Fig. 2). Therefore, we conclude that the magnetorotational instability is responsible for generating the mean poloidal magnetic flux.

Extended Data Fig. 5 plots meridional profiles of the mean radial magnetic field $\bar{B}_r$ at selected time slices for the simulation with $\Delta x_{\text{finest}} = 12.5$ (200) m in the left (right) column (see also the visualization: http://www2.yukawa.kyoto-u.ac.jp/~kenta.kiuchi/anime/SAKURA/movie_Mean_Poloidal_Flux.mp4). It is evident that the mean poloidal field is generated in the region where the magnetorotational instability is active ($\rho \lesssim 10^{14.5}$ g cm^{-3}), particularly, in the low-latitude region $0.24 \lesssim \theta \lesssim 0.5\pi$. Then, it propagates towards the high-latitude region and generates the jet. We also point out that at a radius of 9–10 km, the polar region has a weak magnetic field. This indicates that the poloidal field below this region does not contribute towards the launch of a jet and stays buried throughout the simulation.

The low-resolution simulation also shows some amplification of the mean poloidal field in the low-density region with $\rho \lesssim 10^{12}$ g cm^{-3}, where the magnetorotational instability is resolved. (see the visualizations for the mean poloidal flux and magnetorotational instability quality factor in the simulation with $\Delta x_{\text{finest}} = 200$ m: http://www2.yukawa.kyoto-u.ac.jp/~kenta.kiuchi/anime/SAKURA/movie_Mean_Poloidal_Flux_Low.mp4 and http://www2.yukawa.kyoto-u.ac.jp/~kenta.kiuchi/anime/SAKURA/movie_Mean_MRI_Qfac_Low.mp4). It shows qualitatively similar behaviour to the simulation with $\Delta x_{\text{finest}} = 12.5$ m, but the efficiency for generating the mean poloidal magnetic field is much lower, which leads to a weaker Poynting flux luminosity (see the 'Detailed properties of the Poynting-flux-dominated outflow and magnetically driven post-merger ejecta' section).

$\alpha\Omega$ dynamo

To understand the dynamo process in the simulation, we used the mean field theory with an axisymmetric average. We consider an axisymmetric average because it corresponds to the symmetry of the differential rotation in the system. In the mean field dynamo theory, we assume that the velocity field **U** and the magnetic field **B** are, respectively, composed of the mean velocity field $\bar{\textbf{U}}$ and velocity fluctuations **u** so that $\textbf{U} = \bar{\textbf{U}} + \textbf{u}$ and of the mean magnetic field $\bar{\textbf{B}}$ and the magnetic fluctuations **b**. We then average the induction equation, which gives equation (1), where $\bar{\mathcal{E}} = \overline{\textbf{u} \times \textbf{b}}$ is the electromotive force due to the fluctuations. To close the system, the electromotive force is often expressed as a function of the mean magnetic field, and its spatial derivatives as described by equation (2). α_{ij} and β_{ij} are, respectively, tensors expressing the contributions of the mean magnetic field $\bar{\textbf{B}}$ and its derivatives $\bar{\textbf{J}} = \nabla \times \bar{\textbf{B}}$ to the electromotive force. These tensors

should not depend on $\bar{\textbf{B}}$. First, we focus on how the mean poloidal field is generated and then look at the toroidal field.

To show how the mean poloidal field is generated by the alpha or beta effect, we assume that the mean velocity field is composed of the rotation speed $\bar{\textbf{U}} = R\Omega\textbf{e}_\phi$ and project the averaged induction equation (1) in the radial direction in cylindrical coordinates, which gives:

$$\partial_t \bar{B}_R = -\partial_z \left[(\bar{\textbf{U}} \times \bar{\textbf{B}})_\phi + \bar{\mathcal{E}}_\phi \right] = -\partial_z \bar{\mathcal{E}}_\phi = -\partial_z \left(\alpha_{\phi j} \bar{B}_j + \beta_{\phi j} (\nabla \times \bar{\textbf{B}})_j \right). \quad (12)$$

Similarly, by projecting the averaged induction equation in the vertical direction, the generation of the mean vertical field $\bar{B}_z$ is due to the azimuthal component of the electromotive force $\bar{\mathcal{E}}_\phi$. For the generation of the mean toroidal field, the Ω effect (that is the winding of the magnetic field by differential rotation) is also important and must be compared to the contributions of both the radial and vertical components of the electromotive force $\bar{\mathcal{E}}_R$ and $\bar{\mathcal{E}}_z$. To estimate which of the mean magnetic field $\bar{B}_i$ or the derivatives of the mean magnetic field $\bar{J}_i$ contributes the most to the electromotive force $\bar{\mathcal{E}}_i$, we compute the Pearson correlation coefficients between the quantities $\bar{\mathcal{E}}_i$ and $Y_j = \bar{B}_j$ or $\bar{J}_j$ with the following formula:

$$\mathcal{C}_{\text{P}}(\bar{\mathcal{E}}_i, Y_j) = \frac{\int_t (\bar{\mathcal{E}}_i - \langle \bar{\mathcal{E}}_i \rangle_t)(Y_j - \langle Y_j \rangle_t)\, \text{d}t}{\sqrt{\left(\int_t (\bar{\mathcal{E}}_i - \langle \bar{\mathcal{E}}_i \rangle_t)^2\, \text{d}t \right)} \sqrt{\left(\int_t (Y_j - \langle Y_j \rangle_t)^2\, \text{d}t \right)}}, \quad (13)$$

where $\langle \cdot \rangle_t$ represents a time average.

In the following sections, we present a complementary analysis of the other contributions to the generation of the mean magnetic field than the $\alpha_{\phi\phi}$ effect and Ω effect. We, therefore, show the other correlations between the electromotive force and the magnetic field and the estimated values of the tensor component. Several methods can be used for the values of the alpha tensor components. The simplest one is to estimate them from the correlations[23], but this method assumes that one component is dominant. To take into account the off-diagonal contributions, we compute the values of the alpha tensor coefficients in this study by using a singular value decomposition in a least-squares fit of the mean current data and mean field[66].

Generation of the mean poloidal field $\bar{B}_R$. As shown in equation (12), the generation of the axisymmetric poloidal field is due to the curl of the toroidal component of the electromotive force in the averaged induction equation. In this section, we show the correlations between the toroidal electromotive force $\bar{\mathcal{E}}_\phi$ and the magnetic field components $\bar{B}_j$ and the mean current $\bar{J}_j$ (top and middle panels of Extended Data Fig. 6). The low correlations with the mean current $\bar{J}_j$ shows that its contributions to $\bar{\mathcal{E}}_\phi$ (that is the β_{ij} tensor) can be neglected. In the same way, the vertical magnetic field contribution $\bar{B}_z$ can be neglected. Extended Data Fig. 6 also shows the anti-correlation of $\bar{B}_\phi$ and $\bar{\mathcal{E}}_\phi$ and also that the radial magnetic field $\bar{B}_R$ is correlated to $\bar{\mathcal{E}}_\phi$. This is because the radial field $\bar{B}_R$ is anti-correlated to the toroidal magnetic field $\bar{B}_\phi$ due to the Ω effect (Fig. 3). Since the mean toroidal field $\bar{B}_\phi$ is anti-correlated to the toroidal electromotive force $\bar{\mathcal{E}}_\phi$, the mean radial field $\bar{B}_R$ is correlated to it. To confirm that the contribution of $\bar{B}_\phi$ dominates, we first compute the non-diagonal components of the alpha tensor (bottom panel of Extended Data Fig. 6). We then compare the contribution of $\bar{B}_\phi$ and $\bar{B}_R$, that is, respectively, the time-averaged values of $\alpha_{\phi\phi}\bar{B}_\phi$ and $\alpha_{\phi R}\bar{B}_R$ in the first 10 km:

$$\frac{\langle \alpha_{\phi\phi} \bar{B}_\phi \rangle_t}{\langle \alpha_{\phi R} \bar{B}_R \rangle_t} = 1.87. \quad (14)$$

Generation of the mean toroidal field. In the main text, we show that the Ω effect is important for the generation of the mean toroidal field. In this section, we check whether the contribution of the α effect

through the poloidal components of the electromotive force $\bar{\mathcal{E}}_R$ and $\bar{\mathcal{E}}_z$ is substantial, in which case the dynamo is called an $\alpha^2\Omega$ dynamo instead of an $\alpha\Omega$ dynamo. First, we confirm that the correlations between the electromotive force and the mean current $\bar{J}_j$ (right panels of Extended Data Fig. 7) are lower than with the mean magnetic field $\bar{B}_j$ (left panels of Extended Data Fig. 7). The contributions from the mean current can, therefore, be neglected. For the mean magnetic field, some components, for example, the mean toroidal field $\bar{B}_\phi$, are strongly correlated with the radial component of the electromotive force $\bar{\mathcal{E}}_R$. This indicates that the α effect might be important to the generation of the mean toroidal field. To compare the strength of these two effects, the α effect and the Ω effect, we computed the corresponding α tensor components α_{Ri} and α_{zi} and estimated the ratio of the two dynamo numbers $C_\alpha = \max(|\alpha_{Ri}|, |\alpha_{zi}|)R/\eta$ for $i \in [R, \phi, z]$ and $C_\Omega = \Omega R^2/\eta$, where η is the resistivity, in the turbulent region averaged for one scale height, which gives at $R = 30$ km:

$$\frac{C_\Omega}{C_\alpha} = \frac{\Omega R}{\max(|\alpha_{Ri}|, |\alpha_{zi}|)} \approx 30.8. \qquad (15)$$

The contribution of the α effect to the generation of the mean toroidal field can, therefore, be reasonably neglected as the Ω effect dominates the generation of the mean toroidal field. The dynamo in our simulation can, therefore, be interpreted as an $\alpha\Omega$ dynamo.

Detailed properties of the Poynting-flux-dominated outflow and magnetically driven post-merger ejecta

The link http://www2.yukawa.kyoto-u.ac.jp/~kenta.kiuchi/anime/SAKURA/DD2_135_135_Dynamo.mp4 is a visualization for the rest-mass density (top left), the magnetic field strength (top, second from left), the magnetization parameter (top, second from right), the unbound-edness defined by the Bernoulli criterion (top right), the electron fraction (bottom left), the temperature (bottom, second from left), the entropy per baryon (bottom, second from right) and the geodesic criterion (bottom right) on a plane perpendicular to the orbital plane.

The top panel of Extended Data Fig. 8 plots the angular distribution of the luminosity of the Poynting flux, which is calculated as follows:

$$L_{\text{Poynting}}(\theta) = -\int_{r\approx 500\text{km}} \alpha\psi^6 r^2 (T^r{}_t)_{\text{(EM)}}\, d\phi, \qquad (16)$$

where α and ψ are the lapse function and the conformal factor, respectively. The high luminosity of $\sim 2\text{–}8 \times 10^{52}$ erg s^{-1} angle^{-1} is confined in a region with $\theta < 12°$.

The middle panel plots the jet-opening-angle-corrected luminosity and luminosity of the Poynting flux (green and blue, respectively) as functions of the post-merger time. According to refs. [67–69], the luminosity of the Poynting-flux-dominated outflow, which is driven by the efficient magnetic winding from the remnant of the binary neutron star merger, can be estimated as

$$L_{\text{Poy}} =$$
$$\int L_{\text{Poynting}}(\theta)\sin\theta\, d\theta \approx 10^{51}\, \text{erg s}^{-1}\left(\frac{\bar{B}_P}{10^{15}\,\text{G}}\right)^2\left(\frac{R}{10^6\,\text{cm}}\right)^3\left(\frac{\Omega}{8,000\,\text{rad s}^{-1}}\right), \qquad (17)$$

where $\bar{B}_P$ is the azimuthally averaged poloidal magnetic field. In the current simulation, it is $\sim 10^{15}$ G. Thus, the Poynting flux luminosity found in the simulation is consistent with this estimation. The jet-opening-angle-corrected luminosity is $\sim 10^{52}$ erg s^{-1}. Thus, if we assume that the conversion efficiency to gamma-ray photons is $\sim 10\%$, it is compatible with the observed luminosity of short, hard gamma-ray bursts[42].

The bottom panel plots the ejecta as a function of the post-merger time. The solid curve denotes the result from using the Bernoulli criteria. The coloured region in the inset shows the error of the baryon mass conservation, which is below $10^{-7} M_\odot$ throughout the simulation.

Convergence study and effect of the initial large-scale magnetic field

Because we chose an initial large-scale magnetic field strength that is much stronger than those observed in binary pulsars[36], we need to clarify whether such a strong large-scale field is responsible for launching the jet.

We begin by estimating the magnetic winding timescale originating from the initial magnetic field. Suppose we consider a binary neutron star merger with a highly magnetized end of 10^{11} G, as observed for pulsars. In that case, the timescale for the magnetic winding to reach saturation is

$$\bar{B}_\phi \approx 10^{16.5}\,\text{G}\left(\frac{\bar{B}_R}{5 \times 10^{11}\,\text{G}}\right)\left(\frac{\Omega}{8,000\,\text{rad s}^{-1}}\right)\left(\frac{t}{8\,\text{s}}\right), \qquad (18)$$

where we assume that the compression due to the merger amplifies the initial poloidal field by a factor of five, which should be proportional to $\rho^{2/3}$ because of conservation of the magnetic flux. We also assume a saturation field strength of $10^{16.5}$ G, as suggested by the super-high-resolution simulation (Extended Data Fig. 1). Therefore, the magnetic winding originating from the initial magnetic field should be minor or irrelevant in reality.

However, the magnetic winding timescale is much shorter than those in reality in both simulations with $\Delta x_{\text{finest}} = 12.5$ or 200 m because of the assumed strong initial field. The low-resolution mesh is fine enough to resolve the compression and winding but can only partially capture the Kelvin–Helmholtz and the magnetorotational instability. Therefore, there would be no striking difference between the simulations for the jet launching mechanism if such a strong initial poloidal field and subsequent magnetic winding were responsible for it. The middle panel of Extended Data Fig. 8 shows that the Poynting-flux-dominated outflow is launched at $t - t_{\text{merger}} \approx 60$ ms and reaches $\sim 10^{49-50}$ erg s^{-1} in the low-resolution simulation with $\Delta x_{\text{finest}} = 200$ m. However, in the same plot, the super-high-resolution simulation with $\Delta x_{\text{finest}} = 12.5$ m shows that the Poynting-flux-dominated outflow is launched at $t - t_{\text{merger}} \approx 35$ ms. The luminosity reaches $\sim 10^{51}$ erg s^{-1}. The difference is striking. As discussed in Extended Data Fig. 5, the efficiency of the generation of the mean poloidal flux in the super-high-resolution simulation is much higher than that in the low-resolution simulation. This indicates that the efficient $\alpha\Omega$ dynamo is responsible for launching the strong jet.

The bottom panel of Extended Data Fig. 8 also suggests that the Lorentz force-driven post-merger ejecta is launched in the run with $\Delta x_{\text{finest}} = 200$ m. However, the ejecta mass is about one order of magnitude smaller than in the run with $\Delta x_{\text{finest}} = 12.5$ m, showing that the enhanced activity of magnetohydrodynamics effects by the efficient dynamo action plays an important role in ejecting matter[21].

Data availability

The raw simulation data (265TB) that support the findings of this study are available from the corresponding author upon request. The prerequisite for a data request is having a server where the data can be transferred to.

Code availability

The numerical relativity code and data analysis tool are available from the corresponding author upon reasonable request.

References

1. Abbott, B. P. et al. Multi-messenger observations of a binary neutron star merger. *Astrophys. J. Lett.* **848**, L12 (2017).
2. Goldstein, A. et al. An ordinary short gamma-ray burst with extraordinary implications: Fermi-GBM detection of GRB 170817A. *Astrophys. J. Lett.* **848**, L14 (2017).
3. Savchenko, V. et al. INTEGRAL detection of the first prompt gamma-ray signal coincident with the gravitational-wave event GW170817. *Astrophys. J. Lett.* **848**, L15 (2017).

4. Mooley, K. P. et al. Superluminal motion of a relativistic jet in the neutron-star merger GW170817. *Nature* **561**, 355 (2018).

5. Abbott, B. P. et al. GW170817: observation of gravitational waves from a binary neutron star inspiral. *Phys. Rev. Lett.* **119**, 161101 (2017).

6. Metzger, B. D. et al. Electromagnetic counterparts of compact object mergers powered by the radioactive decay of *r*-process nuclei. *Mon. Not. R. Astron. Soc.* **406**, 2650 (2010).

7. Lattimer, J. M. & Schramm, D. N. Black-hole–neutron-star collisions. *Mon. Not. R. Astron. Soc.* **192**, L145 (1974).

8. Eichler, D., Livio, M., Piran, T. & Schramm, D. N. Nucleosynthesis, neutrino bursts and γ-rays from coalescing neutron stars. *Nature* **340**, 126 (1989).

9. Wanajo, S. et al. Production of all the *r*-process nuclides in the dynamical ejecta of neutron star mergers. *Astrophys. J. Lett.* **789**, L39 (2014).

10. Shibata, M. et al. Modeling GW170817 based on numerical relativity and its implications. *Phys. Rev. D* **96**, 123012 (2017).

11. Kasen, D. et al. Origin of the heavy elements in binary neutron-star mergers from a gravitational wave event. *Nature* **551**, 80 (2017).

12. Metzger, B. D., Thompson, T. A. & Quataert, E. A magnetar origin for the kilonova ejecta in GW170817. *Astrophys. J.* **856**, 101 (2018).

13. Fujibayashi, S. et al. Mass ejection from the remnant of a binary neutron star merger: viscous-radiation hydrodynamics study. *Astrophys. J.* **860**, 64 (2018).

14. Perego, A., Radice, D. & Bernuzzi, S. AT 2017gfo: an anisotropic and three-component kilonova counterpart of GW170817. *Astrophys. J. Lett.* **850**, L37 (2017).

15. Waxman, E., Ofek, E. O., Kushnir, D. & Avishay, G.-Y. Constraints on the ejecta of the GW170817 neutron-star merger from its electromagnetic emission. *Mon. Not. R. Astron. Soc.* **481**, 3423 (2018).

16. Kawaguchi, K., Shibata, M. & Tanaka, M. Radiative transfer simulation for the optical and near-infrared electromagnetic counterparts to GW170817. *Astrophys. J. Lett.* **865**, L21 (2018).

17. Breschi, M. et al. AT2017gfo: Bayesian inference and model selection of multicomponent kilonovae and constraints on the neutron star equation of state. *Mon. Not. R. Astron. Soc.* **505**, 1661 (2021).

18. Villar, V. A. et al. The combined ultraviolet, optical, and near-infrared light curves of the kilonova associated with the binary neutron star merger GW170817: unified data set, analytic models, and physical implications. *Astrophys. J. Lett.* **851**, L21.

19. Ruiz, M., Shapiro, S. L. & Tsokaros, A. GW170817, general relativistic magnetohydrodynamic simulations, and the neutron star maximum mass. *Phys. Rev. D* **97**, 021501 (2018).

20. Fernández, R. et al. Long-term GRMHD simulations of neutron star merger accretion discs: implications for electromagnetic counterparts. *Mon. Not. R. Astron. Soc.* **482**, 3373 (2019).

21. Mösta, P. et al. A magnetar engine for short GRBs and kilonovae. *Astrophys. J. Lett.* **901**, L37 (2020).

22. Brandenburg, A. & Subramanian, K. Astrophysical magnetic fields and nonlinear dynamo theory. *Phys. Rep.* **417**, 1 (2005).

23. Reboul-Salze, A., Guilet, J., Raynaud, R. & Bugli, M. MRI-driven αΩ dynamos in protoneutron stars. *Astron. Astrophys.* **667**, A94 (2022).

24. Shibata, M., Fujibayashi, S. & Sekiguchi, Y. Long-term evolution of a merger-remnant neutron star in general relativistic magnetohydrodynamics: effect of magnetic winding. *Phys. Rev. D* **103**, 043022 (2021).

25. Mösta, P. et al. A large scale dynamo and magnetoturbulence in rapidly rotating core-collapse supernovae. *Nature* **528**, 376 (2015).

26. Metzger, B. D. et al. The proto-magnetar model for gamma-ray bursts. *Mon. Not. R. Astron. Soc.* **413**, 2031 (2011).

27. Hayashi, K. et al. General-relativistic neutrino-radiation magnetohydrodynamic simulation of seconds-long black hole-neutron star mergers. *Phys. Rev. D* **106**, 023008 (2022).

28. Gottlieb, O. et al. Large-scale evolution of seconds-long relativistic jets from black hole–neutron star mergers. *Astrophys. J. Lett.* **954**, L21 (2023).

29. Christie, I. M. et al. The role of magnetic field geometry in the evolution of neutron star merger accretion discs. *Mon. Not. R. Astron. Soc* **490**, 4811 (2019).

30. Blandford, R. D. & Znajek, R. L. Electromagnetic extractions of energy from Kerr black holes. *Mon. Not. R. Astron. Soc* **179**, 433 (1977).

31. Kiuchi, K., Kyutoku, K., Sekiguchi, Y. & Shibata, M. Global simulations of strongly magnetized remnant massive neutron stars formed in binary neutron star mergers. *Phys. Rev. D* **97**, 124039 (2018).

32. Kiuchi, K., Held, L. E., Sekiguchi, Y. & Shibata, M. Implementation of advanced Riemann solvers in a neutrino-radiation magnetohydrodynamics code in numerical relativity and its application to a binary neutron star merger. *Phys. Rev. D* **106**, 124041 (2022).

33. Hempel, M. & Schaffner-Bielich, J. Statistical model for a complete supernova equation of state. *Nucl. Phys. A* **837**, 210–254 (2010).

34. Fujibayashi, S. et al. Postmerger mass ejection of low-mass binary neutron stars. *Astrophys. J.* **901**, 122 (2020).

35. Kiuchi, K. et al. Efficient magnetic-field amplification due to the Kelvin–Helmholtz instability in binary neutron star mergers. *Phys. Rev. D* **92**, 124034 (2015).

36. Lorimer, D. R. Binary and millisecond pulsars. *Living Rev. Rel.* **11**, 8 (2008).

37. Price, D. J. & Rosswog, S. Producing ultrastrong magnetic fields in neutron star mergers. *Science* **312**, 719 (2006).

38. Rasio, F. A. & Shapiro, S. L. Coalescing binary neutron stars. *Class. Quantum Gravity* **16**, R1 (1999).

39. Balbus, S. A. & Hawley, J. F. A powerful local shear instability in weakly magnetized disks. I. Linear analysis. *Astrophys. J.* **376**, 214 (1991).

40. Parker, E. A. Hydromagnetic dynamo models. *Astrophys. J.* **122**, 293 (1955).

41. Yoshimura, H. Solar-cycle dynamo wave propagation. *Astrophys. J.* **201**, 740 (1975).

42. Fong, W. et al. A decade of short-duration gamma-ray burst broadband afterglows: energetics, circumburst densities, and jet opening angles. *Astrophys. J.* **815**, 102 (2015).

43. Metzger, B. D., Quataert, E. & Thompson, T. A. Short-duration gamma-ray bursts with extended emission from protomagnetar spin-down. *Mon. Not. R. Astron. Soc.* **385**, 1455 (2008).

44. Drenkhahn, G. & Spruit, H. C. Efficient acceleration and radiation in Poynting flux powered GRB outflows. *Astron. Astrophys.* **391**, 1141 (2002).

45. Blandford, R. D. & Payne, D. G. Hydromagnetic flows from accretion discs and the production of radio jets. *Mon. Not. R. Astron. Soc.* **199**, 883 (1982).

46. Tanaka, M. & Hotokezaka, K. Radiative transfer simulations of neutron star merger ejecta. *Astrophys. J.* **775**, 113 (2013).

47. Metzger, B. D., Piro, A. L. & Quataert, E. Neutron-rich freeze-out in viscously spreading accretion disks formed from compact object mergers. *Mon. Not. R. Astron. Soc.* **396**, 304 (2009).

48. Salvesen, G., Simon, J. B., Armitage, P. J. & Mitchell, C. Accretion disc dynamo activity in local simulations spanning weak-to-strong net vertical magnetic flux regimes. *Mon. Not. R. Astron. Soc.* **457**, 857 (2016).

49. Palenzuela, C. et al. Turbulent magnetic field amplification in binary neutron star mergers. *Phys. Rev. D* **106**, 023013 (2022).

50. Aguilera-Miret, R., Palenzuela, C., Carrasco, F. & Viganò, D. The role of turbulence and winding in the development of large-scale, strong magnetic fields in long-lived remnants of binary neutron star mergers. *Phys. Rev. D.* **108**, 103001 (2023).

51. Shibata, M. & Namamura, T. Evolution of three-dimensional gravitational waves: harmonic slicing case. *Phys. Rev. D* **52**, 5428–5444 (1995).

52. Baumgarte, T. W. & Shapiro, S. L. On the numerical integration of Einstein's field equations. *Phys. Rev. D* **59**, 024007 (1998).

53. Baker, J. G. et al. Gravitational wave extraction from an inspiraling configuration of merging black holes. *Phys. Rev. Lett.* **96**, 111102 (2006).

54. Campanelli, M., Lousto, C. O., Marronetti, P. & Zlochower, Y. Accurate evolutions of orbiting black-hole binaries without excision. *Phys. Rev. Lett.* **96**, 111101 (2006).

55. Hilditch, D. et al. Compact binary evolutions with the Z4c formulation. *Phys. Rev. D* **88**, 084057 (2013).

56. Mignone, A., Ugliano, M. & Bodo, G. A five-wave HLL Riemann solver for relativistic MHD. *Mon. Not. R. Astron. Soc.* **393**, 1141 (2009).

57. Gardiner, T. A. & Stone, J. M. An unsplit Godunov method for ideal MHD via constrained transport in three dimensions. *J. Comput. Phys.* **227**, 4123–4141 (2008).

58. Sekiguchi, Y., Kiuchi, K., Kyotoku, K. & Shibata, M. Current status of numerical-relativity simulations in Kyoto. *Prog. Theor. Exp. Phys.* **2012**, 01A304 (2012).

59. http://www.lorene.obspm.fr/

60. Timmes, F. X. & Swesty, F. D. The accuracy, consistency, and speed of an electron–positron equation of state based on table interpolation of the Helmholtz free energy. *Astrophys. J. Suppl.* **126**, 501 (2000).

61. Aguilera-Miret, R., Viganò, D., Carrasco, F., Miñano, B. & Palenzuela, C. Turbulent magnetic-field amplification in the first 10 milliseconds after a binary neutron star merger: comparing high-resolution and large-eddy simulations. *Phys. Rev. D* **102**, 103006 (2020).

62. Aguilera-Miret, R., Viganò, D. & Palenzuela, C. Universality of the turbulent magnetic field in hypermassive neutron stars produced by binary mergers. *Astrophys. J. Lett.* **926**, L31 (2022).

63. Chandrasekhar, S. *Hydrodynamic and Hydromagnetic Stability* (Clarendon, 1961).

64. Viganò, D. et al. General relativistic MHD large eddy simulations with gradient subgrid-scale model. *Phys. Rev. D* **101**, 123019 (2020).

65. Guilet, J., Bauswein, A., Just, O. & Janka, H. T. Magnetorotational instability in neutron star mergers: impact of neutrinos. *Mon. Not. R. Astron. Soc.* **471**, 1879 (2016).

66. Racine, É. et al. On the mode of dynamo action in a global large-eddy simulation of solar convection. *Astrophys. J.* **735**, 46 (2011).

67. Meier, D. L. A magnetically switched, rotating black hole model for the production of extragalactic radio jets and the Fanaroff and Riley class division. *Astrophys. J.* **522**, 753 (1999).

68. Shibata, M., Suwa, Y., Kiuchi, K. & Ioka, K. Afterglow of a binary neutron star merger. *Astrophys. J. Lett.* **734**, L36 (2011).

69. Kiuchi, K., Kyotoku, K. & Shibata, M. Three dimensional evolution of differentially rotating magnetized neutron stars. *Phys. Rev. D* **86**, 064008 (2012).

Acknowledgements

Author contributions

K.K. and A.R.S. were the primary drivers of the project and wrote the main text and method sections and developed the figures. M. S., Y. S. and K.K. were the primary developers of the numerical relativity code, which was written from scratch. K.K. performed the numerical relativity simulations. A.R.S. analysed the simulation data. M.S. prepared the infrastructure for the large-scale numerical computations. All authors were involved in interpreting and discussing the results and in commenting on or editing the text.

Funding

Competing interests

The authors declare no competing interests.

Additional information

Extended data Extended are available for this paper at https://doi.org/10.1038/s41550-024-02194-y.

Correspondence and requests for materials should be addressed to Kenta Kiuchi.
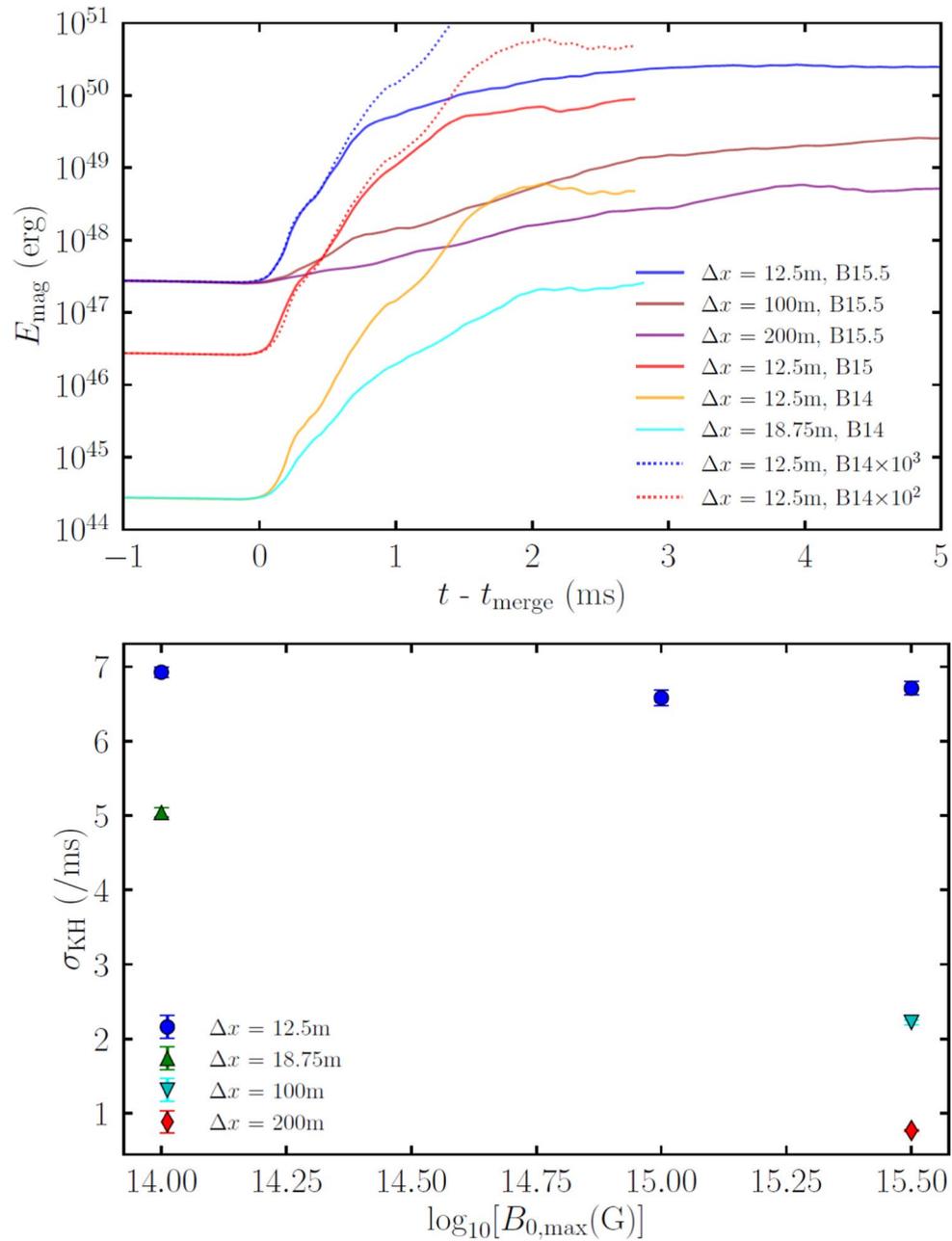
Peer review information *Nature Astronomy* thanks the anonymous reviewers for their contribution to the peer review of this work.

Reprints and permissions information is available at www.nature.com/reprints.

Publisher's note Springer Nature remains neutral with regard to jurisdictional claims in published maps and institutional affiliations.

**Extended Data Fig. 1 | Kelvin-Helmholtz instability growth rate at the merger.** (Top) Same as the inset in Fig. 1 in the main article, but with $\Delta x_{\text{finest}} = 18.75$ m for $B_{0,\text{max}} = 10^{14}$ G (cyan). The blue- and red-dotted curves show the evolution for $\Delta x_{\text{finest}} = 12.5$ m and $B_{0,\text{max}} = 10^{14}$ G magnified by a factor of 10^3 and 10^2, respectively. (Bottom) Dependence of the growth rate of the electromagnetic energy at the merger due to the Kelvin-Helmholtz instability on the initial magnetic field strength $B_{0,\text{max}}$ and grid resolution. The error is due to the fitting. Data are presented as mean median values +/- SD.
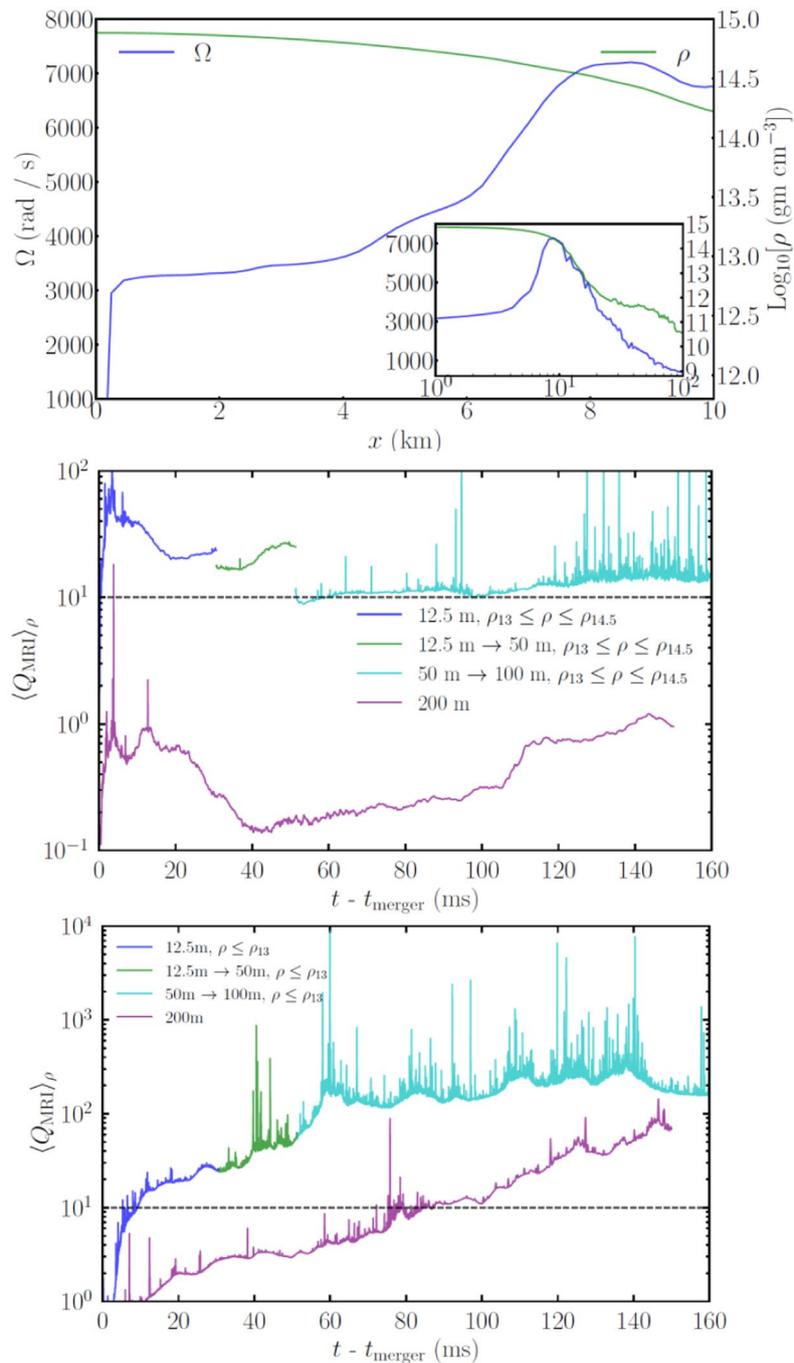
Extended Data Fig. 2 | Magnetorotational instability inside the merger remnant. (Top) The radial profile of the angular velocity (blue) and the rest-mass density (green) on the equatorial plane at $t - t_{\rm merger} \approx 50$ ms. Magnetorotational instability is inactive in a region with $x \lesssim 9$ km and $\rho \gtrsim 10^{14.5}$ g/cm³. The inset shows the same profiles with the logarithmic scale in the radial direction. (Middle) Magnetorotational instability quality factor in a core region as a function of time. The remnant core is defined by a region with $\rho \geq 10^{13}$ g/cm³. The blue curve denotes the employed finest grid resolution of 12.5 m. At $t - t_{\rm merger} \approx 30$ ms, the two finest domains with $\Delta x_{\rm finest} = 12.5$ m and $\Delta x_{\rm finest} = 25$ m are removed. Thus, the employed grid resolution is $\Delta x_{\rm finest} = 50$ m plotted with the green curve. At $t - t_{\rm merger} \approx 50$ ms, the finest domain with $\Delta x_{\rm finest} = 50$ m is removed and the subsequent evolution with $\Delta x_{\rm finest} = 100$ m is plotted with the cyan curve. The result with $\Delta x_{\rm finest} = 200$ m is plotted with the purple curve. (Bottom) The same as the middle panel, but for a torus defined by a region with 10^7 g/cm³ $\leq \rho \leq 10^{13}$ g/cm³.
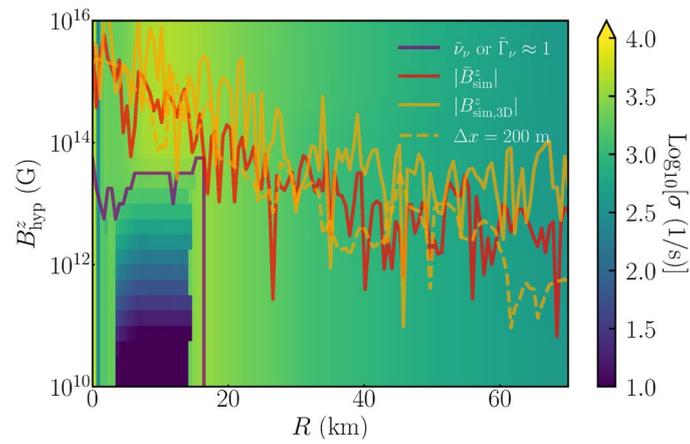
Extended Data Fig. 3 | Neutrino viscosity and drag on the magnetorotational instability. Growth rate of the fastest growing mode of the neutrino viscous/drag magnetorotational instability as a function of the radius of the remnant massive neutron star and the hypothetical value of the z-component of the magnetic field B^z_{hyp}. We take the simulation data on the orbital plane at $t - t_{\mathrm{merger}} \approx 10$ ms. The purple curve denotes the boundary where $\tilde{\nu}_\nu$ or $\tilde{\Gamma}_\nu \approx 1$. Outside the boundary, the growth rate is essentially the same as the ideal magnetorotational instability. The red curve denotes the z-component of the azimuthally averaged magnetic field strength in the simulation. The orange-solid (dashed) curve denotes the three-dimensional data for the z-component on the $x = 0$ axis in the simulation with $\Delta x_{\mathrm{finest}} = 12.5(200)$ m.
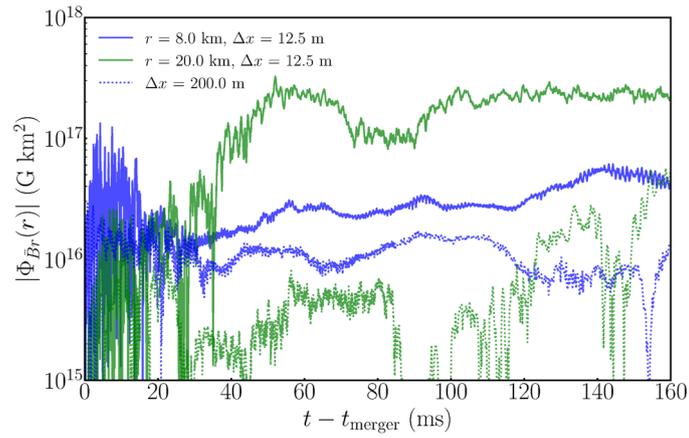
Extended Data Fig. 4 | Generation of the mean poloidal-magnetic flux inside the merger remnant. Mean poloidal-magnetic flux as a function of the time after the merger. Blue and green-solid curves denote the flux on the sphere of $r = 8$ and 20 km, respectively, which are representative for the magnetorotational instability inactive and active region, in the simulation with $\Delta x_{\mathrm{finest}} = 12.5$ m. The dashed counterparts denote the simulation with $\Delta x_{\mathrm{finest}} = 200$ m.
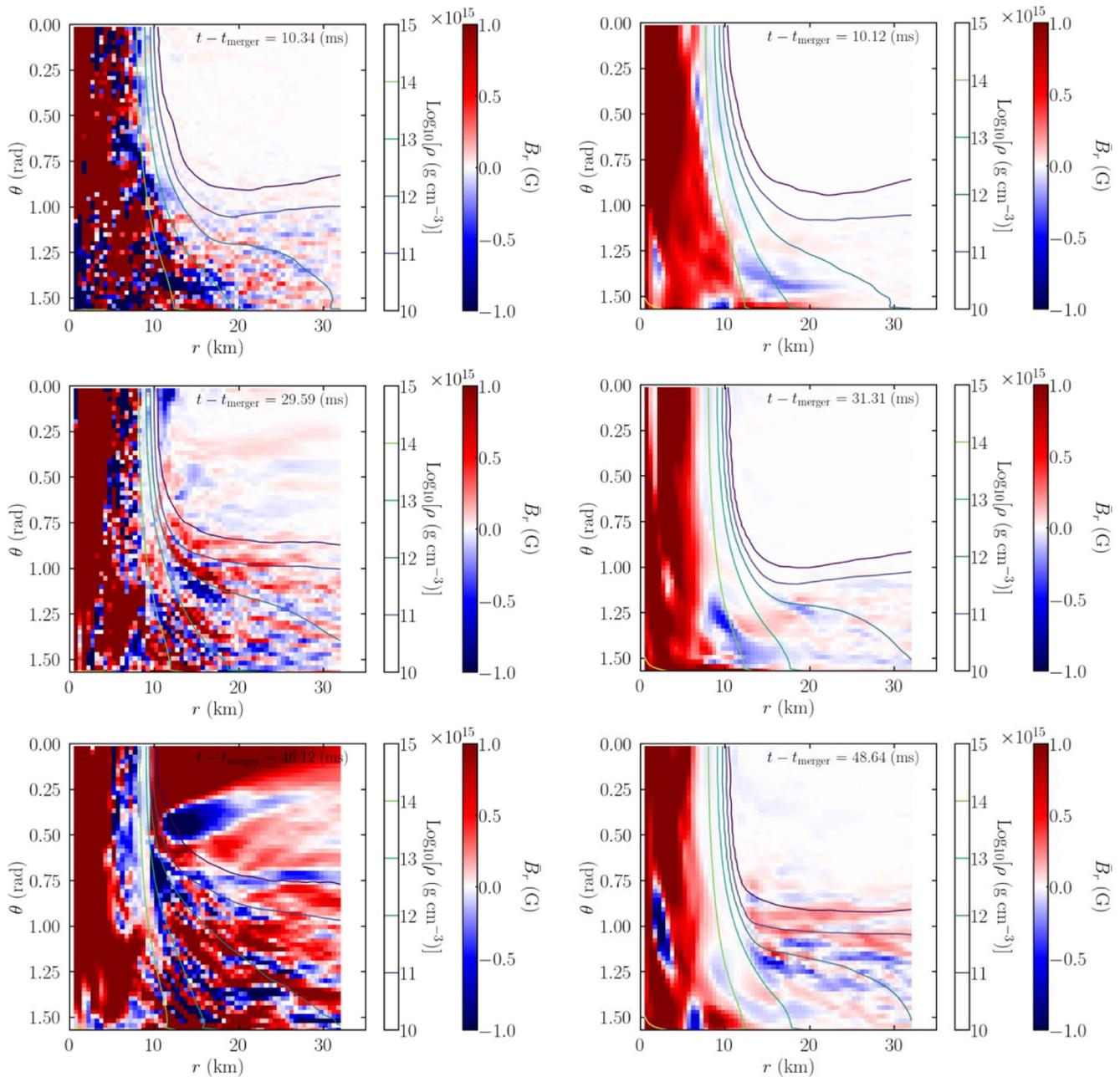
Extended Data Fig. 5 | Generation of the mean radial magnetic field.
Meridional profile of the mean radial magnetic field, $\bar{B}_r$, at ≈ 10 ms (top),
30 ms (center), and 50 ms (bottom) for the simulation with $\Delta x_{\mathrm{finest}} = 12.5$ m
(left column) and 200 m (right column). The rest-mass density contour
curves are also plotted. The visualization is the following link
(http://www2.yukawa.kyoto-u.ac.jp/~kenta.kiuchi/anime/SAKURA/movie_
Mean_Poloidal_Flux.mp4) for the super-high resolution simulation, and
http://www2.yukawa.kyoto-u.ac.jp/~kenta.kiuchi/anime/SAKURA/movie_
Mean_Poloidal_Flux_Low.mp4 for the low-resolution simulation.
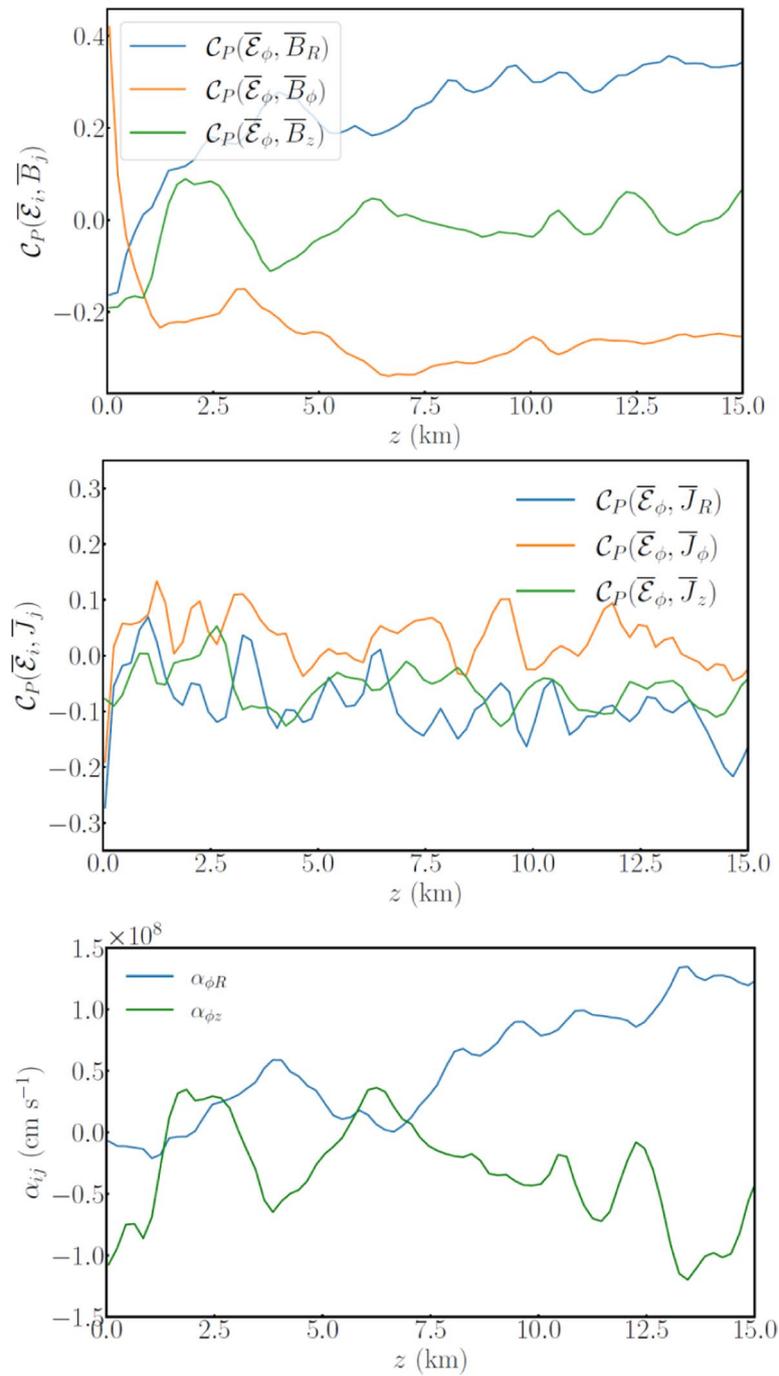
Extended Data Fig. 6 | α effect vs turbulent resistivity in the αΩ dynamo. (Top) Time-averaged correlations between the toroidal electromotive force $\bar{\mathcal{E}}_\phi$ and the mean magnetic field components $\bar{B}_j$ for $R = 30$ km. (Middle) Time-averaged correlations between the toroidal electromotive force $\bar{\mathcal{E}}_\phi$ and the mean current $\bar{J}_j$ components for $R = 30$ km. (Bottom) Alpha tensor components $\alpha_{\phi i}$ with $i \in [R, z]$ for $R = 30$ km.
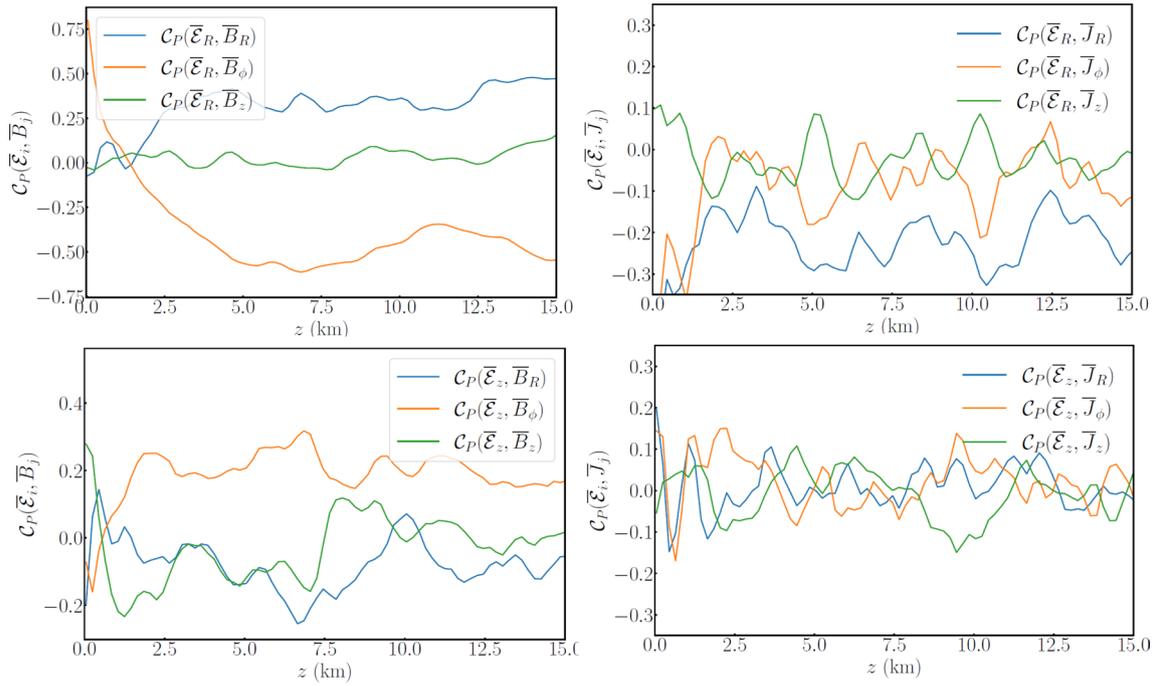
Extended Data Fig. 7 | $\alpha\Omega$ vs $\alpha^2\Omega$ dynamo. (Left) Time-averaged correlations between the poloidal electromotive force $\bar{\mathcal{E}}_R$ (top) and $\bar{\mathcal{E}}_z$ (bottom) and mean magnetic field components $\bar{B}_i$ for $R = 30$ km. (Right) Time-averaged correlations between the poloidal electromotive force $\bar{\mathcal{E}}_R$ (top) and $\bar{\mathcal{E}}_z$ (bottom) and mean current components $\bar{J}_i$ for $R = 30$ km.
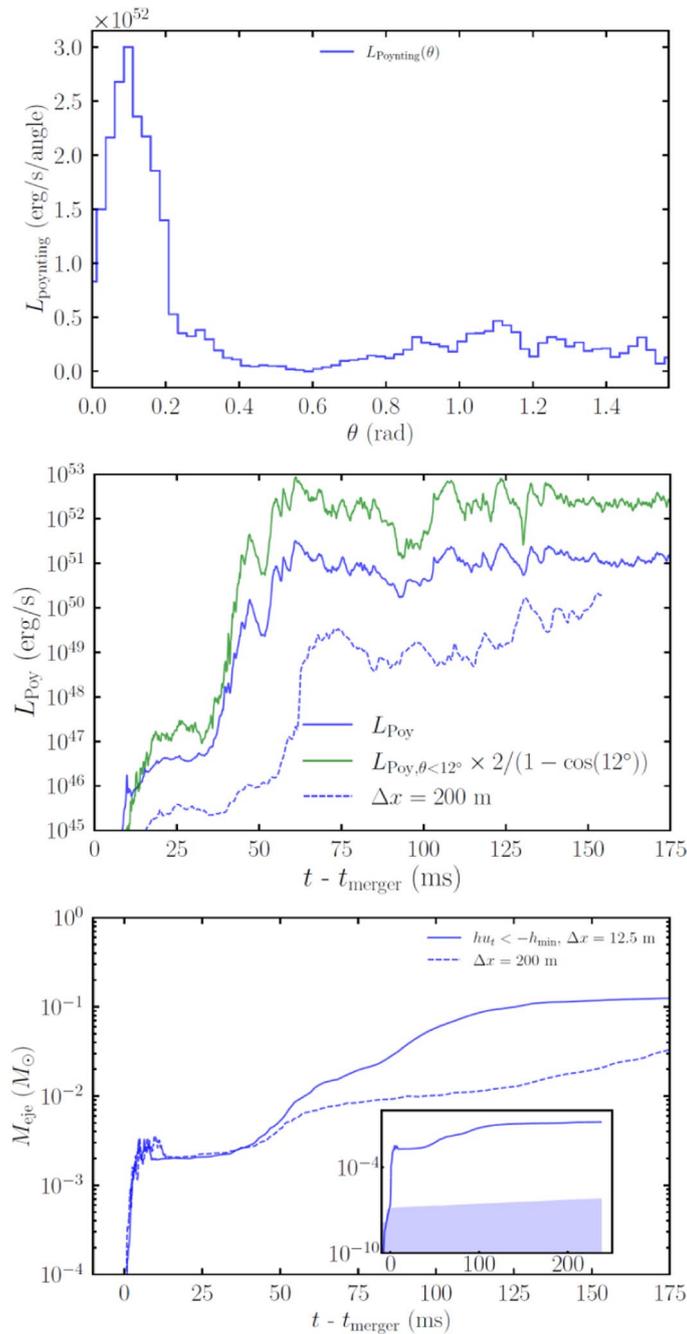
Extended Data Fig. 8 | Properties of the Poynting flux-dominated outflow and post-merger ejecta. (Top) Angular distribution of the luminosity of the Poynting flux at the end of the simulation of $t - t_{merger} \approx 150$ ms. (Middle) Luminosity for the Poynting flux as a function of the post-merger time. The green curve is the jet-opening-angle corrected luminosity. The blue-dashed curve plots the luminosity for the simulation with $\Delta x_{finest} = 200$ m. (Bottom) Ejecta as a function of the post-merger time. The solid curve denotes the ejecta satisfying the Bernoulli criterion. The colored region in the inset shows the violation of the baryon mass conservation. The blue-dashed curve plots the ejecta for the simulation with $\Delta x_{finest} = 200$ m.